JACS
JOURNAL OF THE AMERICAN CHEMICAL SOCIETY

Article

pubs.acs.org/JACS

A Quantum Chemical Interpretation of Two-Dimensional Electronic Spectroscopy of Light-Harvesting Complexes

Francesco Segatta,[†,‡] Lorenzo Cupellini,[¶] Sandro Jurinovich,[¶] Shaul Mukamel,[§] Maurizio Dapor,[†] Simone Taioli,[†,∥] Marco Garavelli,*[,‡] and Benedetta Mennucci*[,¶]

[†]European Center for Theoretical Studies in Nuclear Physics and Related Areas (ECT*-FBK) and Trento Institute for Fundamental Physics and Applications (TIFPA-INFN), 38123 Trento, Italy

[‡]Dipartimento di Chimica Industriale "Toso Montanari", University of Bologna, Viale del Risorgimento, 4, 40136 Bologna, Italy

[¶]Dipartimento di Chimica e Chimica Industriale, University of Pisa, via G. Moruzzi 13, 56124 Pisa, Italy

[§]Department of Chemistry, University of California, Irvine, California 92697-2025, United States

[∥]Faculty of Mathematics and Physics, Charles University, Prague 116 36, Czech Republic

Supporting Information

ABSTRACT: Nonlinear electronic spectroscopies represent one of the most powerful techniques to study complex multichromophoric architectures. For these systems, in fact, linear spectra are too congested to be used to disentangle the many coupled vibroelectronic processes that are activated. By using a 2D approach, instead, a clear picture can be achieved, but only when the recorded spectra are combined with a proper interpretative model. So far, this has been almost always achieved through parametrized exciton Hamiltonians that necessarily introduce biases and/or arbitrary assumptions. In this study, a first-principles approach is presented that combines accurate quantum chemical descriptions with state-of-the-art models for the environment through the use of atomistic and polarizable embeddings. Slow and fast bath dynamics, along with exciton transport between the pigments, are included. This approach is applied to the 2DES spectroscopy of the Light-Harvesting 2 (LH2) complex of purple bacteria. Simulations are extended over the entire visible-near-infrared spectral region to cover both carotenoid and bacteriochlorophyll signals. Our results provide an accurate description of excitonic properties and relaxation pathways, and give an unprecedented insight into the interpretation of the spectral signatures of the measured 2D signals.

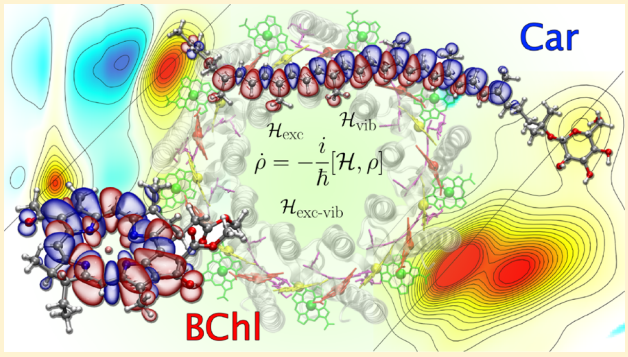

1. INTRODUCTION

Advances in electronic spectroscopy with femtosecond time resolution, such as the two dimensional electronic spectroscopy (2DES), have provided new insight into the energy transfer processes in the light-harvesting (LH) pigment−protein complexes present in photosynthetic organisms.[1−4] The high complexity of these systems, where multiple interacting pigments are embedded in a protein matrix, leads to extremely intricate energy landscapes due to the interplay of excitonic, vibronic and, eventually, charge-transfer states. By spreading signals along two frequency axes and following the dynamics of excitation with very high time resolution, the 2DES technique allows one to disentangle the overlapping transient spectra. As a result, a high density of information is obtained, but to objectively disentangle all these features and reach a detailed and reliable map of the energy transfer network is still a challenge. A possible strategy to solve the latter issue is to integrate the measurements with theoretical models: this has been successfully done by combining calculations, data extracted from experiments, and tunable parameters.[5−8] Attempts of more sophisticated quantum chemical approaches to the simulation of 2DES were conducted on the Fenna−Matthews−Olson complex,[9] however these rely on semi-empirical calculations of key quantities.

Here we present an accurate quantum-chemistry based multiscale approach to simulate 2DES spectra of multi-chromophoric systems in complex environments for a direct comparison with experiments. By combining two different levels of quantum chemistry (density functional theory and multireference perturbative RASSCF/RASPT2) with two classical embedding schemes (electrostatic and polarizable) to account for the environment, we calculate all quantities needed to build up the exciton−phonon model with a unified theoretical framework able to incorporate slow and fast bath dynamics, along with exciton transport between the pigments. Because of its ab initio character, our approach represents an unambiguous strategy to achieve a clear interpretation of the

Received: March 2, 2017
Published: May 17, 2017

DOI: 10.1021/jacs.7b02130
J. Am. Chem. Soc. 2017, 139, 7558−7567

spectra even when many different pigments are involved and a large range of wavelengths has to be explored. By switching on and off selected interactions among pigments, a detailed molecular-level analysis of the intricate network of couplings between the multiple electronic processes and the intra/intermolecular nuclear degrees of freedom can be achieved.

We demonstrate the potential of our approach by simulating the 2DES spectroscopy at low (77 K) and room temperature of one of the most challenging system, namely the main LH complex of purple bacteria, the Light-Harvesting 2 (LH2) of *Rps. acidophila*. Since the determination of its high-resolution structural model reported in 1995 by Cogdell and co-workers,[10] LH2 has been extensively studied with different experimental techniques (see ref 11 for a recent exhaustive review). Many theoretical studies have also been performed;[6,8,12−20] however, the accurate interpretation of the excitonic properties of this highly symmetric system is still disputed, mostly owing to the different coupling regimes, which are active on the same time.

The LH2 complex is characterized by a cylindrical C_9 structure, containing 27 bacteriochlorophylls *a* (BChl) and 9 carotenoids (Car) as absorbing pigments.[21] The BChls are organized in two rings, a closely packed ring (B850) containing 18 BChls whose molecular plane is perpendicular to the cylinder radius, and a more loosely packed ring (B800) that contains 9 BChls, whose molecular plane is perpendicular to the C_9 axis (See Figure 1). The backbone of the Car molecules (Rhodopin Glucoside) encompasses the whole polypeptide chain and bridges the two BChl rings.

Due to this unique structural arrangement, the bright Q_y excitations of the B850 BChls are strongly coupled, whereas those of the B800 BChls are more weakly coupled; the coupling between the two rings is also not negligible. This is reflected in the near IR characteristic signal arising from delocalized Q_y excitons. When we move to the region where the Q_x transition of the BChls and/or the bright state of the carotenoids are excited, the couplings decrease significantly in both rings as well as between the BChl rings and the connecting Cars.

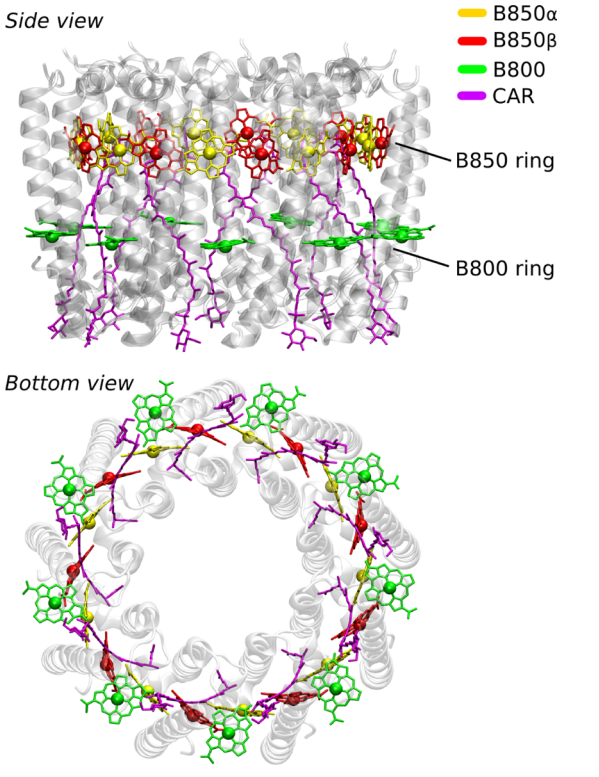

Figure 1. Molecular structure of LH2. Pigments are highlighted using the following color code: yellow for BChl B850*α*, red for B850*β*, green for B800, purple for the Carotenoid.

For the first time, the present simulation is extended over the entire Car-Q_x plus Q_y visible-near-infrared (VIS-NIR) region. Due to the very different coupling regimes, the exciton model is combined with Redfield and Modified Redfield theories[22−25] to describe exciton relaxation within delocalized states of the Q_y region, and the Förster theory within the Car-Q_x region.

Our results are compared with recently published experimental 2DES data,[26,27] showing the importance of previously unaddressed aspects of the modeling and revealing new aspects of the recorded signals.

Focusing on the Q_y region, the good agreement between experimental and theoretical maps, obtained when the Coulomb interaction of the full transition densities and the polarization effects of the environment are included, points out to the importance of a proper evaluation of the intra and inter-ring couplings. Moreover, we show that the simulations must include the excitation and detection pulse envelopes in order to achieve a quantitative agreement of the simulated intensities of B800 and B850 bands with experimentally recorded 2D maps.

Moving to the Car-Q_x region of the 2D map, the calculations clearly identify the signals due to the combined effect of the vibronic progression of the Car's bright S_2 state and BChl's Q_x transition, respectively. This is particularly important for those off-diagonal peaks that were used to reveal the presence of a previously postulated carotenoid dark state of the same symmetry of S_2,[28] which lies in between S_2 and Q_x states. The comparison between simulated and measured spectra reveals which signals are due to vibronic progression of BChl's Q_x which can be labeled as pure vibrational progressions of the bright Car S_2 state, and which should indeed be recognized as Car signatures coming from states other than S_2.

2. STRUCTURE AND METHODS

We used the crystal structure of LH2 (PDB code: 1NKZ) resolved at 2.0 Å.[29] To ensure a C_9 symmetry, we considered a single monomer, which was replicated over the symmetry axis. All details regarding the structure preparation are reported in Section S1 of the Supporting Information.

The multichromophoric system is described in terms of an exciton Hamiltonian

$$\hat{H} = \sum_i \epsilon_i |i\rangle\langle i| + \sum_{ij} V_{ij} |i\rangle\langle j| \quad (1)$$

where ϵ_i is the excited-state energy of the *i*-th chromophore, and V_{ij} is the electronic coupling between chromophores *i* and *j*. We considered separate Hamiltonians for (i) the near-infrared region of the spectrum, which includes the Q_y transitions of BChls, and (ii) the visible region, which contains contributions from the bright (S_2) states of Cars and the Q_x states of BChls.

The elements of the exciton Hamiltonian were computed using a hybrid QM/MM model to account for the effect of the protein environment. In particular, we employed two levels of QM theory, i.e., time-dependent density functional theory (TD-DFT) with the CAM-B3LYP functional,[30] and the RASSCF/RASPT2 methodology,[31,32] with different Active Spaces (AS) and State Average (SA) settings in the two different regions of the spectrum (see Section S5 of the Supporting Information). The TD-DFT based calculations were performed within both an electrostatic (MM) and a polarizable embedding (MMPol). In the latter model, the environment is

DOI: 10.1021/jacs.7b02130
J. Am. Chem. Soc. 2017, 139, 7558−7567

described as a set of atomic point charges and isotropic atomic polarizabilities.[33] The RAS calculations were performed within the electrostatic embedding of fixed point charges. Higashi et al. showed CAM-B3LYP to be inaccurate for the description of solvatochromic shifts when coupled with an electrostatic embedding, and proposed to tune the range-separation parameter.[34,35] However, the exciton structure obtained in ref 19 with CAM-B3LYP/MMPol well reproduced the exciton splitting of the B850 ring, therefore CAM-B3LYP is appropriate for describing excitation with a polarizable embedding. Further details on the quantum chemical calculations are reported in Section S2 of the Supporting Information.

The electronic couplings in the TD-DFT/MMPol scheme were computed as the Coulomb interaction between the transition densities of the interacting moieties.[36] Note that the polarizable environment adds an explicit screening term to the Coulomb coupling.[33] In the RASSCF/RASPT2/MM approach, the Coulomb couplings were computed with the transition density cube (TDC) method,[37] where no explicit screening is included. It has been shown, both theoretically[19] and experimentally,[38] that the nearest-neighbor Q_y couplings in the B850 ring are reduced with increasing temperature; for this reason, in order to reproduce the room-temperature properties, we used the exciton Hamiltonian calculated by some of the present authors along a classical molecular dynamics (MD) trajectory.[19]

The full set of excitonic parameters (site energies and couplings) used is reported in sections S7 and S8 of the Supporting Information.

In order to describe exciton−phonon couplings, the spectral densities (SD) of the different transitions were modeled as a sum of one overdamped Brownian oscillator[39] and M discrete contributions. The discrete part of the SD, which accounts for the intramolecular vibrations of the various molecules, was determined from a normal-mode analysis[40] of the pigments in the crystal structure, and typical values[6] were adapted for the continuous part. Different spectral densities were explicitly used for the Q_y transitions of B850 α, B850 β and B800 molecules, but we used an average spectral density for all Q_x transitions. All details and parameters are reported in Section S4 of the Supporting Information.

To describe spectra and dynamics within the Q_y region, we employed the disordered exciton model with both standard Redfield (sR) and modified Redfield (mR) theories.[22,25] This choice is natural if one considers the strongly coupled B850 pigments; moreover, mR theory has shown to compare well against nonperturbative hierarchical equations for the simulation of the linear spectra of the B800 ring.[15] Spectra and dynamics within the Car-Q_x region were described by Förster theory. This is justified by the large reorganization energy of the Cars and by the considerable energy gap between Cars and Q_x states. Static disorder in the transition energies of the various pigments was taken into account by averaging the optical properties on a Gaussian distribution of site energies. Further details about the choice of the exciton dynamics theory are reported in Section S3 of the Supporting Information.

2DES pump−probe spectra were simulated within the *supermolecule* or Sum Over States (SOS) approach,[41,42] using site energies, couplings and transition dipole moments either from TD-DFT or RAS based computations, and accounting for different experimental set-ups in the different spectral regions investigated. We adopted a spectral line shape model that incorporates slow and fast bath dynamics, together with exciton transport between the chromophores.[41,43] The 2D signals, which depend parametrically on the three controlled excitation-pulse time delays t_1, t_2 and t_3, are displayed in the frequency domain by performing a 2D Fourier transform along t_1 and t_3, while keeping the waiting time (or population time) t_2 fixed. Unless otherwise specified, the 2DES maps are calculated at $t_2 = 0$ fs. We considered only those double excitations that are associated with combinations of electronic states in the single-exciton manifold, all higher lying states were not included in the simulation. We further refined the spectra by including the pulse envelopes and polarizations (See Section S3 of the Supporting Information).

All TD-DFT and RAS calculations as well as all spectra simulations have been performed using an in-house modified version of Gaussian G09,[44] MOLCAS 8.1[45] and Spectron 2.7,[41] respectively.

3. RESULTS AND DISCUSSION

For clarity the presentation of the results is divided into two sections, one referring to the Q_y region, for which standard and modified Redfield theories were used, and the other focused on the Car-Q_x region, for which the Förster theory was employed.

3.1. The Q_y Region. The exciton Hamiltonians for the Q_y region calculated with alternative strategies (namely RASSCF/RASPT2/MM, TD-DFT/MM, and TD-DFT/MMPol) are detailed in Table S4 of the Supporting Information. The absolute values of the site energies obtained on the crystal structure with the two different QM levels (RASSCF/RASPT2 and TD-DFT) are generally quite similar (within 600 cm^{-1}) when the same electrostatic embedding model is used (MM). The introduction of a more refined polarizable embedding (MMPol) leads to a significant red-shift, due to the inductive effects of the protein residues surrounding the pigments.[46] Some differences between the QM levels are instead found in the relative ordering of the site energies for the different BChls: in particular, TD-DFT models give B800 as the most blue-shifted, while in the RASSCF/RASPT2 calculations B800 is found between B850 α and β. This different behavior, which is not due to the embedding model, as both TD-DFT/MM and TD-DFT/MMPol give the same trend, is related to the different electronic description by the two QM levels at slightly different internal geometries of the BChls.

The specific embedding model has a significant effect on the couplings: for example, the inverted behavior and the different magnitude of the $V^1_{\alpha\beta}$ and the $V^2_{\alpha\beta}$ coupling values (Table S4) in the two different levels of QM theory can safely be attributed to the screening effect,[19] included only in the TD-DFT/MMPol calculations through the polarizable embedding. As expected, this screening plays a significant role in determining the coupling between BChls within the B850 ring where the BChls are closely packed.

By using the three different Hamiltonians, the linear spectra generated as described in the Structure and Methods section are reported in Figure 2.

Due to differences in the absolute site energies in the different QM methods, the computed spectra were shifted individually by a different amount, in order to compare with experiment. As expected, RASSCF/RASPT2 level of QM description gives a more accurate estimation of the site energies, and the corresponding spectrum requires only a small (120 cm^{-1}) shift to the blue to match the experimental B800 peak. A much larger blue-shift is necessary at the TD-DFT level. However, in spite of the larger offset in the absolute energies, the TD-DFT/MMPol approach better reproduces the band splitting between the two peaks at 800 and 850 nm, due to a more balanced description of site energy differences and couplings. The latter, in fact, correctly accounts for the possible screening effects as a polarizable embedding (MMPol) has been used. For this reason, we employed TD-DFT/MMPol data to model the 2DES maps.

In Figure 3 we report the simulated 2DES maps at zero population time and temperatures 77 K (Figure 3d) and 300 K (Figure 3e), along with the experimental map (Figure 3f) of the bacterium *Rps. palustris*[27] in the same spectral region, acquired at zero population time and 300 K. The 77 K 2DES map was computed using the TD-DFT/MMPol Hamiltonian calculated

DOI: 10.1021/jacs.7b02130
J. Am. Chem. Soc. 2017, 139, 7558−7567

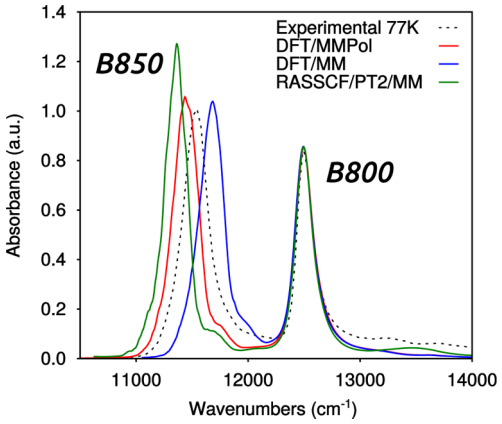

Figure 2. Comparison of linear absorption spectra of the Q_y region computed at 77 K, using modified Redfield theory, at different levels of QM theory and/or embedding models. The experimental spectrum is also reported (dashed line).[47] The calculated spectra have been shifted to match the experimental peak at 800 nm. The TD-DFT/MMPol, TD-DFT/MM and RASSCF/RASPT2/MM spectra have been shifted by 1280, 550, and 120 cm^{-1}, respectively.

on the crystal structure, whereas for the 300 K map we employed the MD Hamiltonian from ref 19. The pulse shapes were designed in order to resemble the experimental pulse envelopes (approximately the same overlap with the various bands as it appears in the experimental spectrum).

The simulated maps at the two temperatures show a similar positioning of peaks and cross-peaks, but, as expected, the 77 K map is dominated by the site energy static disorder (peaks extended along the diagonal), while the 300 K map shows much broader peaks. We observe a considerable similarity between simulated and experimental maps at 300 K especially in the relative position, shape and intensity of the positive and negative B850 signals. To this respect, it has been shown by Fleming et al.[48] that the positioning of these positive and negative B850 related features can be used as a coarse-grained probe for structural insights on the studied system. Symmetrically, when the structure is already known (such as for the LH2 of *Rps. acidophila*), the correct reproduction of positioning, shapes and relative intensities of these features supplies an indirect proof of the accuracy of both the underlying quantum chemical method and the spectra simulation protocols used. With regard to B800 signals, strong excited state absorption (ESA) signals on both sides of the main diagonal are present in the experiment, whereas the same signals appear to be weaker in the computed maps. We note that our simulated ESA signals only arise from combinations of electronic states in the single-exciton manifold; thus, we did not include ESA signals related to the excitation of the higher lying Soret bands from the Q_y transition. As the frequency of such excitations is compatible with these negative ESA on both sides of the positive bleaching, it is possible that $Q_y \rightarrow$ Soret excitations contribute to the negative signals around the diagonal B800 peak. Furthermore, it should also be noted that calculations and experiments refer to different bacteria even if they present a high similarity in both the linear absorption and circular dichroism spectra.[47]

A good agreement between experimental and theoretical maps can be found also in the off-diagonal regions, with similar positive and negative features in both sides of the maps. The presence of these off-diagonal signals in the spectra reflects the weak but still non-negligible coupling between the excitons of the two rings, which is accurately taken into account in our QM/MMPol model. In fact, these off-diagonal signals are present also in the rephasing maps measured by Harel and Engel for the LH2 of *Rb. sphaeroides*.[49] We reported the simulated rephasing 2DES map for the LH2 of the *Rps. acidophila* in Figure S12 of the Supporting Information: the

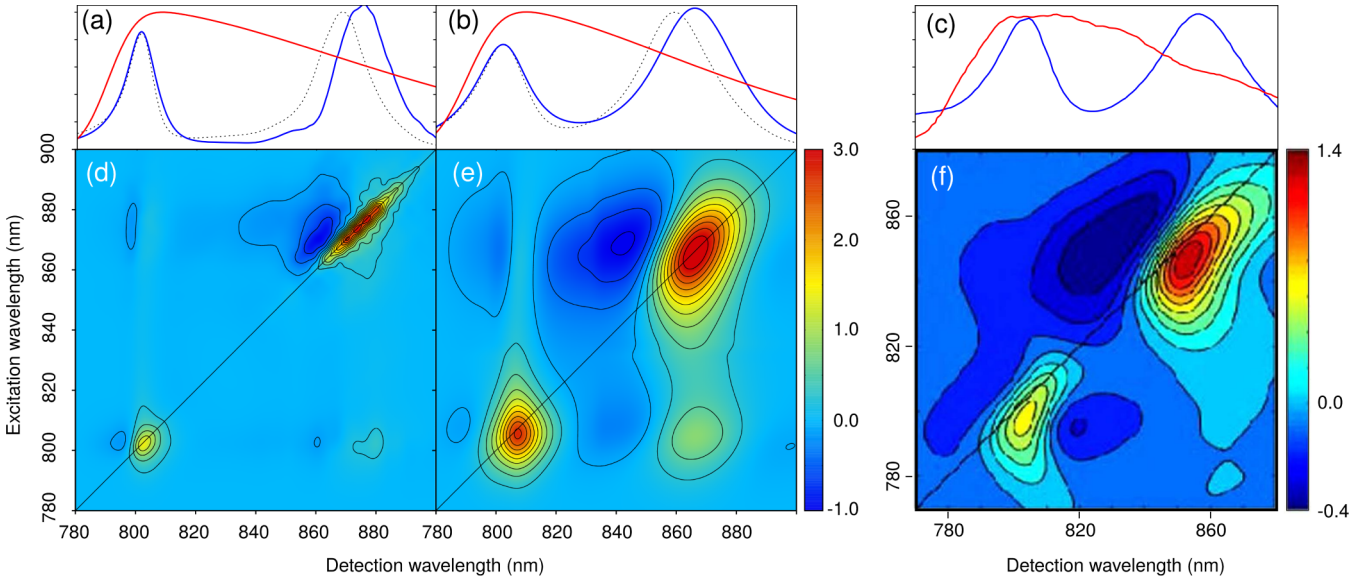

Figure 3. Comparison of 2DES pump−probe maps at zero population time. Simulated maps at 77 K (d) were computed for the TD-DFT/MMPol Hamiltonian. Simulated maps at 300 K (e) were computed for the MD Hamiltonian.[19] In both cases the modified Redfield theory of transport was employed. All simulated maps were shifted to match the experimental peak at 800 nm. The experimental map at 300 K (f) refers to the LH2 of *Rps. palustris*.[27] The corresponding linear absorptions (blue) and pulse shapes (red), along with the relative experimental linear spectra (dashed line),[47] are reported in (a), (b) and (c), respectively. Simulated maps are normalized between their minimum and maximum values. By convention, bleach and stimulated emission contributions appear as positive (red) signals, excited state absorption appears as negative (blue) peaks. The experimental map has been adapted from ref 27.

DOI: 10.1021/jacs.7b02130
J. Am. Chem. Soc. 2017, 139, 7558−7567

calculated map clearly shows two off-diagonal signals, which origin from both ground state bleaching and excited state absorption pathways and reveal the exciton coupling between the B800 and B850 rings.

Remarkably, even if all the relevant excited states are properly included in the 2DES simulations, one should also take into account the proper shape of excitation and detection pulses, as implemented here. This refinement is mandatory if, for example, one is interested in comparing the intensities of B800 and B850 bands in simulated and experimentally recorded 2D maps (see Figure S13 of the Supporting Information).

The downhill relaxation rates among the Q_y excitons were analyzed for over 10 000 realizations of static disorder of the site energy distributions, at 77 K and room temperature. For each realization of the disorder, the exciton states were assigned to the B800(B850) ring on the basis of the participation of the B800(B850) pigments to the exciton state. The average relaxation times over 10 000 system realizations of all the rates in each of the three channels (B800 → B800, B800 → B850, and B850 → B850) as well as those obtained averaging just the maximal rate of each channel, are shown in Table 1.

Table 1. Average Transfer Times (in fs) of the LH2 Ring[a]

	77 K	300 K
	Modified Redfield	
B800 → B800	321 (81)	196 (60)
B850 → B850	244 (36)	137 (25)
B800 → B850	1045 (85)	630 (79)
	Redfield	
B800 → B800	317 (100)	168 (64)
B850 → B850	244 (26)	142 (19)
B800 → B850	1032 (79)	670 (65)

[a]Numbers in parentheses refer to the average of maximum rates taken within every realization. Different columns refer to different temperatures. The 300 K rates were computed on the MD Hamiltonian.[19] Only downhill rates have been considered in this analysis.

Calculated B800 → B850 transfer times are around 0.6−1 ps, in line with several experimental findings.[11,21,50−52] The calculated rates depend on temperature, with the mR 300 K rates being 66% faster than the 77 K rates. This is in agreement with the temperature dependence of the B800 → B850 energy transfer in *Rps. acidophila* determined by pump−probe spectroscopy, where the 300 K rate is ∼60% faster than the 77 K rate.[50] Similar measurements on the LH2 of *Rb. sphaeroides* show the same behavior for the inter-ring transfer times.[53] The good reproduction of the temperature dependence of the rates shows the importance of a detailed calculation of the excitonic Hamiltonian for the complex under different conditions.

The intra-B800 relaxation rates are much harder to determine experimentally; anisotropy decay spectroscopy at different temperatures on *Rps. acidophila* shows that the intra-B800 transfer occurs on a 400−800 fs time scale at room temperature,[50] also in agreement with three-pulse photon echo studies.[54] Our intra-B800 300 K transfer rates are faster, indicating the limits of modified Redfield theory in describing the intra-B800 dynamics. Conversely, at 77 K, the calculated rates are much closer to the experiment (240 fs),[50] suggesting that the energy transfer mechanism is different at low and room temperature.

The results also show a weak dependence of the transfer rates on the excitation transfer theory adopted. The main difference between sR and mR theories is that in mR multiple quanta of energy can be exchanged between excitons and phonons, even though sR exciton transfer rates can be larger than mR rates.[24] Modified Redfield reduces to standard Redfield when the site energies approach degeneracy.[24,25] Our results point to a small influence of multiphonon relaxation, for the average relaxation pathways, within our combination of exciton Hamiltonian and energetic fluctuations.

Further insight into the rate analysis can be obtained by investigating the energy dependence of the relaxation rates. In Figure 4 we report two-dimensional histogram plots of the exciton relaxation rate vs exciton energy at 77 K. Notably, the exciton relaxation rates strongly depend on the exciton energy. In the low-energy B850 region (<12 400 cm^{-1}) the exciton relaxation rate rises with the energy; a region with slow relaxation rates can be found around 12 500 cm^{-1}, due to the low-energy end of the B800 band. At the blue edge of the B850 band we notice excitons with a very fast relaxation rate (tens of femtoseconds). We also compared the relaxation rates of the full Q_y sector of the LH2 system with a Hamiltonian where the B800 ring is decoupled from the B850 ring. The comparison with the artificially decoupled system shows that coupling to the B850 states shortens the lifetime (enhances the relaxation rate) of the B800 states. Finally, as the B850 states in this energy region are optically dark, their lifetime can only be measured if these states are mixed with the B800 states. In the

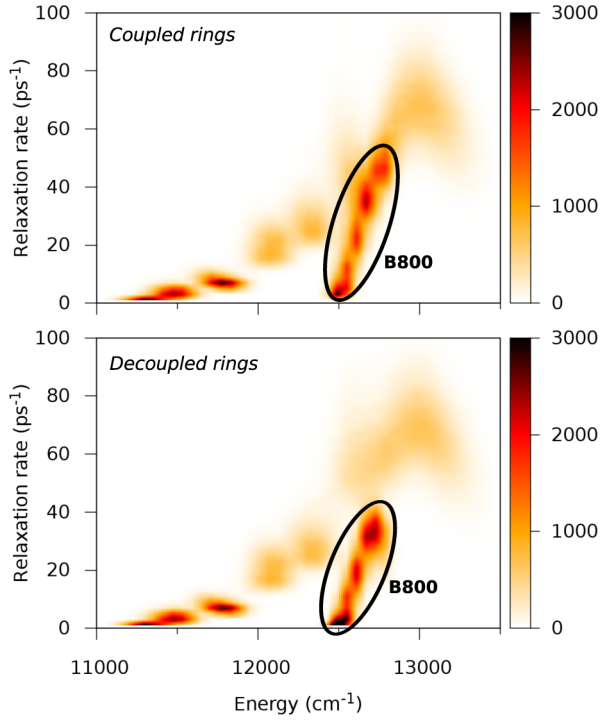

Figure 4. Two-dimensional histogram plots of exciton relaxation rates versus exciton energies (modified Redfield theory using the TD-DFT/MMPol exciton Hamiltonian at 77 K). The histograms show the distribution of energy and relaxation rates over 10 000 realizations of the site energy static disorder. The color range indicates the number of occurrences. The contribution of the B800 states is highlighted with a circle. Top: complete Hamiltonian with coupled rings; bottom: Hamiltonian with the B800 ring decoupled from the B850 ring.

DOI: 10.1021/jacs.7b02130
J. Am. Chem. Soc. 2017, 139, 7558−7567

B800 region the exciton lifetime generally decreases at higher energies. This is in agreement with polarized pump−probe measurements and rate calculations on the LH2 of *Rs. molischianum* at 77 K.[55] Although our computed exciton lifetimes are shorter than the measured polarization relaxation times, it is important to notice that exciton relaxation rates also include processes that may not change the polarization of the transition.[56]

A detailed statistics of delocalization length, dipole strength, and transfer rates in the three lowest exciton states of LH2, which belong to the B850 ring, is reported in Figure S11 of the Supporting Information.

3.2. The Carotenoid-Q_x Region. The Car-Qx linear spectra at both 77 K and 300 K were simulated as described in the Structure and Methods section using the site energies and couplings reported in Table S6 of the SI. Due to the multiexcitation nature of the Car states, only the RASSCF/RASPT2/MM level has been used for the excitonic Hamiltonian in this spectral region, relying on the less expensive TD-DFT computations for the description of the chromophores vibrations (within the spectral densities). The results at both temperatures, together with the experimental spectra, are reported in Figure 5.

The computed spectra, at both 77 K and room temperature, compare well with experiment, showing a similar shape, position and intensity of the absorption bands. Nonetheless, the slight offset in the relative intensities of the Car vibronic peak seems to point to a possible underestimation of the Huang−Rhys factors for the S_2 state, which leads to a general overestimation of the 0−0 transition intensity.

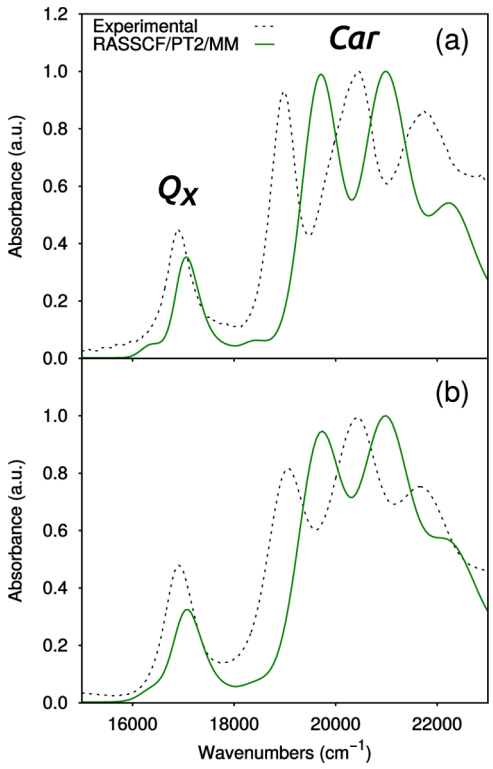

Figure 5. Linear absorption spectra for the Car-Q_x region computed at 77 K (a) and 300 K (b) using Förster transport, at the RASSCF/RASPT2/MM level of theory. The experimental spectra are also reported (dashed line), taken from ref 47. All the spectra have been normalized with respect to the maximum peak. Calculated spectra have not been shifted.

Differently from the Q_y region, available experimental 2D maps in the Car-Q_x region refer exactly to the same photosynthetic organism, namely the *Rps. acidophila*.[26]

In Figure 6, we interpret the origin of experimental signals by artificially disentangling the Car- and BChl-related regions. For such an analysis, we refer to the extrapolated map (corresponding to $t_2 \rightarrow 0$) obtained by Ostroumov et al.[26] through a global target analysis of the measured 2D data.

From the target analysis, the three main diagonal contributions were assigned to ground state bleaching (and stimulated emission) signals from Car S_2 state (full triangle of Figure 6b), BChl Q_x state (empty triangle), and an additional *X* state of Car (empty circle), located in between the S_2 and Q_x transitions. The positive off-diagonal peaks were interpreted as additional signatures in favor of the presence of this elusive Car *X* state: the strong below-diagonal cross-peak (full diamond) was attributed to an ultrafast $S_2 \rightarrow X$ energy transfer, whereas for the above-diagonal cross-peak (empty square) the origin was associated with a ground state bleaching arising from mixed excitation of coupled Q_x and Car *X* states.

We compare these experimental data with our simulated maps consisting, respectively, of purely Car S_2 state signals (Figure 6a), and purely BChl Q_x state contributions (Figure 6c). On the diagonal of the two simulated maps, we observe the bleaching signals of the Car S_2 (full triangle in Figure 6a) and BChl Q_x (empty triangle in Figure 6c) states. We also note that the broad Car S_2 signal has significant contributions along the diagonal toward larger wavelengths, and that an additional diagonal peak around 550 nm (open circle in Figure 6c) is present in the BChl Q_x map. This peak has to be attributed to the direct excitation of the first vibrational state of the 1300−1400 cm^{-1} sequence of modes of the Q_x state, especially the very intense one at 1300 cm^{-1} (see the spectral density reported in Figure S2 of the SI), whose intensity is enhanced by the pulse shape envelopes. A quantification of the effect of this mode on the 2DES map is reported in Figure S14. Our calculations therefore reveal a significant contribution on the diagonal, at the *X* position, deriving from both the broad S_2 bleaching and the Q_x vibronic state, which can in principle explain the observed positive peak.

Moreover, we observe off-diagonal features which can be correlated to experimental signatures, but providing a different interpretation for their origin: the sequence of off-diagonal peaks which appear pumping the Car and probing at larger wavelengths has to be assigned to the S_2 stimulated emission (the full diamond and circle in Figure 6a), and the positive elongations of the experimental Q_x transition, at smaller excitation and detection wavelengths with respect to the bleaching, originate from the vibronic progression of the Q_x (the empty square and diamond in Figure 6c).

The calculated spectra explain the main features of the extrapolated map in terms of the Car bright (S_2) state combined with the Q_x vibronic progression of BChls. We must note, however, that the present theoretical analysis is limited to early t_2 population times without exploiting all the wealth of additional information present at later times to definitely check the validity of the suggested interpretation. Nonetheless, our analysis claims for a necessary review of the interpretation of some of the observed signals, clearly suggesting the importance of previously unaddressed features, such as the Car S_2 stimulated emission signals and the BChl Q_x vibronic

DOI: 10.1021/jacs.7b02130
J. Am. Chem. Soc. 2017, 139, 7558−7567

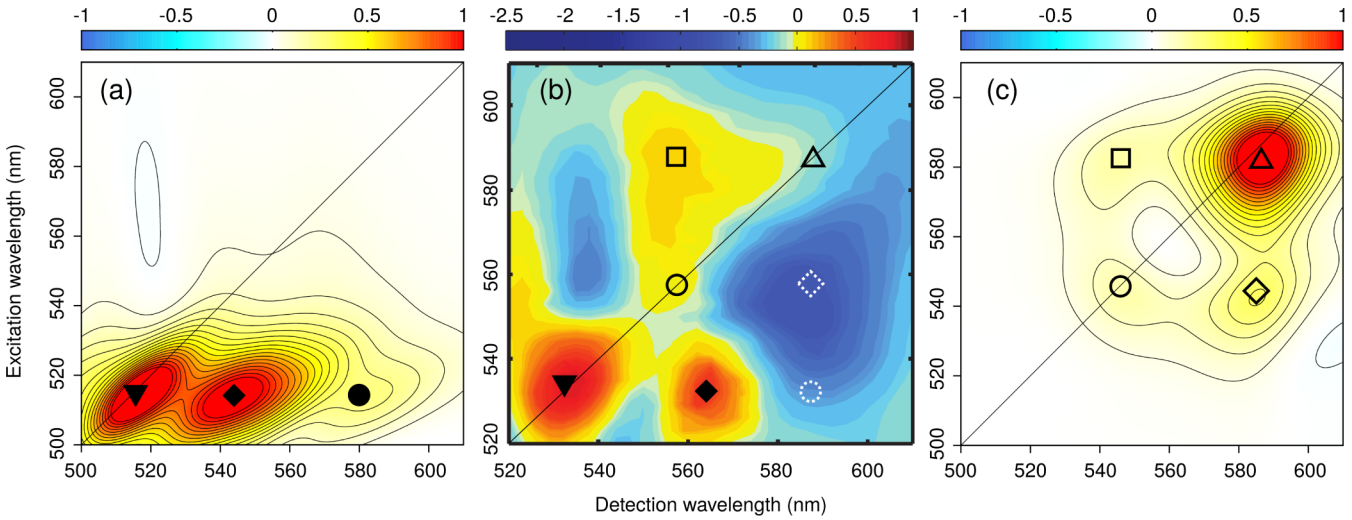

Figure 6. Calculated 2DES pump–probe maps at t_2 = 0 obtained by separately computing Car (a) and BChl (c) contributions. (b) Short t_2 component of the 2D evolutionary-associated spectra obtained through a global target analysis of the experimental 2D data.[26] The effect of the pulse shape has been taken into account in the simulated maps. Simulated maps are normalized to their maximum. By convention bleach and stimulated emission contributions appear as positive (red) signals, excited state absorption appear as negative (blue) peaks. Full (referring to Cars) and empty (referring to BChls) geometric symbols are used to indicate correlations between calculated and measured signals.

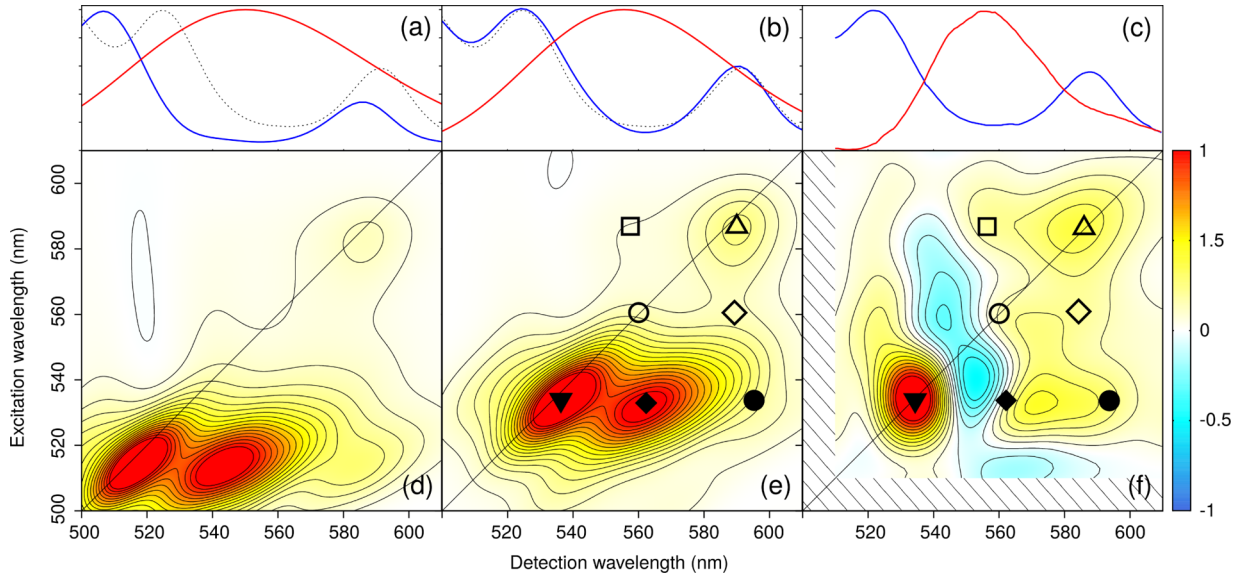

Figure 7. Comparison of simulated (d,e) and experimental[26] (f) 2DES pump–probe maps of *Rps. acidophila* at 300 K and waiting time t_2 = 22 fs. The corresponding linear absorptions (blue) and pulse shapes (red), along with the relative experimental linear spectra (dashed line),[26] are reported in (a), (b) and (c), respectively. In the calculated maps the pulse shape was adapted to have the same overlap between pulses and absorption bands as the one reported in the experiments. Panel (e) refers to a calculated map where Car S_2 site energies and Q_x transition dipoles have been scaled to match the position and the intensities measured in the linear spectrum. Simulated maps are normalized to their maximum. By convention, bleach and stimulated emission contributions appear as positive (red) signals, excited state absorption appears as negative (blue) peaks. The geometric symbols represent the same peaks as in Figure 6.

signatures. The signals on and below the diagonal at the 560 nm excitation wavelength cannot be unambiguously assigned to Car or BChl due to overlaps of the S_2 and Q_x related signatures, indicating the difficulties present in using these peaks for a definitive proof of the Car *X* state. Instead, the peak above the diagonal (indicated with the empty square in Figure 6b) is not significantly affected by any S_2-related signal. The oscillations of this off-diagonal peak have been investigated using a global target analysis of the absorptive 2D signals.[57] The resulting vibration-associated spectra (2DVAS) have been compared to those of the isolated Car and the observed similarity has been used to confirm the Car origin of the signal.

To unify all these theoretical and experimental findings it is necessary to invoke the presence of a Car dark state, either an additional electronic state (the *X* state) or a very hot vibrational level of the low-lying S_1 state. The RASSCF/RASPT2 calculations give an electronic state with the same symmetry of S_2 but lying well above S_2; however, previous multireference DFT calculations[58] have shown that the relative position of the electronic states in Cars strongly depend on the geometry through variations in the bond length alternation. It is thus

DOI: 10.1021/jacs.7b02130
J. Am. Chem. Soc. 2017, 139, 7558–7567

possible that geometrical fluctuations and/or distortions can bring the X state down below the bright one.

Once analyzed the contributions of the two pigments separately, in Figure 7 we report a comparison between the computed Car-Q_x coupled map and the experimental spectrum at early t_2 time (t_2 = 22 fs).

At this short time, the Car region is expected to be dominated by the S_2 state and higher-energy states reached from it. However, some features due to the dark S_1 state cannot be excluded, as assuming an internal conversion process 100−150 fs long, S_1 can still be populated from S_2. Indeed, we note that the negative signals at the red side of the S_2 bleaching, absent in the $t_2 \rightarrow 0$ extrapolated map, and rapidly increasing at larger t_2 times, are likely due to the ESA from both S_2 and S_1. As in our calculations the internal conversion to S_1 is not allowed and both $S_{1\rightarrow n}$ and $S_{2\rightarrow n}$ ESA signals are not included, these negative signals are completely absent. Because these negative signals lower the intensity and modify the shape of the positive S_2 SE, a much more intense and less red-shifted signal is present in the calculated map (see Figure 7). We also observe that the negative signal at increasing excitation wavelengths also contains pure S_2 contributions, since a similar feature also appears in the Car-only simulated map (Figure 6a).

As previously commented for the linear spectra, the relative intensity of the Q_x band with respect to the Car S_2 is weaker in the computed maps compared to the experiment. This difference is even more pronounced in the 2D (Figure 7*d*) due to the multiple interactions between light and the transition dipole moments of the molecules, which characterize this technique. Moreover, the calculated gap between S_2 and Q_x states is slightly too large, leading to a too small spectral overlap between these two signals. To check the effects of these deviations, we have recalculated the 2D map by introducing two corrections: (i) we have introduced a scaling of the Q_x transition dipoles so to match the relative absorption intensities of the experimental linear spectrum, and (ii) we have separately red-shifted the Car S_2 and the BChl Q_x site energies so to match the corresponding measured peaks in the linear spectrum (see the linear spectra reported in Figure 7).

The comparison between the corrected (Figure 7e) and the original calculated 2D maps shows that the main features are fully preserved, telling us that the method used provides a robust description. This is further confirmed by the analysis of the calculated rates of $S_2 \rightarrow Q_x$ energy transfer, obtained applying the Förster theory. These transfers can be separated into three channels, that is, from Car to B800, B850α, and B850β, respectively. The fastest energy transfer occurs to the Q_x state of BChl B850α, which is the most coupled to S_2 (175 cm^{-1} from our calculations).[37] Its EET rate is predicted to be around 140 fs^{-1} (or 110 fs^{-1} if we use the corrected energies). We predict slower EET rates to B800 and B850β, around 1 ps^{-1}. The resulting S_2 depopulation time for EET to Q_x states is ∼120 fs (or 90 fs with the corrected energies). Assuming that the $S_2 \rightarrow S_1$ internal conversion rate of the Car is 130 fs^{-1},[59,60] we estimate a 59% efficiency of energy transfer from the Car to the Q_x states, and a 48% efficiency of EET to B850α alone. These results are in good agreement with several experiments,[59,61] and in particular with the rates estimated from fluorescence upconversion and coupling calculations.[62] Our calculations predict that the Q_x state of B850α is the main energy acceptor from S_2.

4. CONCLUSIONS

Numerous quantum chemical approaches have been employed to describe LH complexes through excitonic models (for a recent review see ref 63). However, the majority of these theoretical investigations concerned linear absorption spectra with very rare extensions to 2DES spectra.[8,9] Furthermore, due to the large size of the multichromophoric aggregate of LH complexes, and the very heterogeneous composition of the embedding, rather approximated QM methods (mostly of semiempirical nature) and/or simplified descriptions of the environment have been generally used. Indeed, the application of ab initio methods have been mostly limited to benchmark studies on the electronic properties of single pigments.[17]

Here, for the first time, the simulation of linear and 2DES spectra of LH2 over the entire Car-Q_x plus Q_y VIS-NIR region has been presented by integrating quantum-chemistry and electron−phonon exciton models. Single and multireference QM methods have been combined with electrostatic and polarizable classical embeddings to properly account for the effect of the protein in all the steps of the simulation. On the one hand, TD-DFT/MMPol computations have been proved to achieve a refined description of the effect of the environment in the Q_y region via a precise reproduction of the B800−B850 bands splitting. On the other hand, the multiconfigurational multireference RASSCF/RASPT2/MM approach provides an accurate description of the Car-Q_x region. All these data were used as input parameters for the construction of exciton Hamiltonians able to describe the manifold of states of the LH2 complex.

In particular, we have shown that, in addition to the molecular components and the accurate description of the environment effects, the modeling of 2D maps must include the pulse envelopes in order to achieve a reliable and complete comparison with experiment. Most importantly, the possibility of artificially switching on and off interactions among the different components of the multichromophoric systems, provides a unique tool for interpreting the origin of the different signals which overlap in the highly congested experimental spectrum. This analysis is especially effective in the Car-Q_x region, where we have given a possible interpretation of the main features of the very-short time 2DES spectrum in terms of the bright S_2 and Q_x vibronic progression of Car and BChl, respectively. By combining these results with those obtained from a global target analysis applied to 2DES data,[57] we have reviewed several observed signals and reinforced the hypothesis that a contribution coming from a dark state of the carotenoid lying in between the S_2 and the Q_x is likely to be present; if this is an additional electronic state (the previously suggested X state) or an high-energy vibrational level of the S_1 is still an open question that calls for further investigation.

We have further shown that the integration of multiscale models and experiments is crucial: only by combining the "independent" results from accurate quantum chemical based methods and detailed 2DES experiments, the complex network of energy transfer routes in LH2 (and in other LH systems) can be definitely revealed. To do that, however, two important improvements are still needed in the theoretical strategy. The ESA signals of Cars, in particular those from S_1, which become increasingly important for longer waiting time, have to be explicitly included to follow the system evolution and simulate time-resolved 2D maps. Moreover, a detailed account of

DOI: 10.1021/jacs.7b02130
J. Am. Chem. Soc. 2017, 139, 7558−7567

possible geometrical distortions of the pigments (especially the Cars) due to temperature-dependent fluctuations of the protein is necessary, as this mechanism could affect the relative energy and the nature of the excited states involved in the excitons and in the energy transfer processes.

■ ASSOCIATED CONTENT

Supporting Information

The Supporting Information is available free of charge on the ACS Publications website at DOI: 10.1021/jacs.7b02130.

Details on the preparation of the structure and the exciton model; Additional details on the calculations of 2DES maps and the treatment of the disorder; Spectral densities of the exciton−phonon coupling; Details of the RASSCF/RASPT2 calculations; Excitonic parameters for both the Q_y and Car-Q_x regions; Analysis of the relaxation rates in the Q_y region; Analysis of the pulse shape and rephasing 2DES map of the Q_y region; Analysis of the Q_x 2DES map (PDF)

■ AUTHOR INFORMATION

Corresponding Authors

*marco.garavelli@unibo.it

*benedetta.mennucci@unipi.it

ORCID

Lorenzo Cupellini: 0000-0003-0848-2908

Marco Garavelli: 0000-0002-0796-289X

Benedetta Mennucci: 0000-0002-4394-0129

Notes

The authors declare no competing financial interest.

■ ACKNOWLEDGMENTS

The authors thank Gregory Scholes and Evgeny Ostroumov for the short-time 2DES map in the Car-Q_x region and for their valuable comments on the comparison of calculated and experimental maps. B.M., S.J. and L.C. acknowledge support by the European Research Council Starting Grant ENLIGHT (ERC-2011-StG No. 277755). M.G. acknowledges support by the European Research Council Advanced Grant STRATUS (ERC-2011-AdG No.291198) and of the French Agence National de la Recherche (FEMTO-2DNA, ANR-15-CE29-0010). S.M. acknowledges the support of the National Science Foundation (Grant CHE-1361516).

■ REFERENCES

(1) Brixner, T.; Stenger, J.; Vaswani, H. M.; Cho, M.; Blankenship, R. E.; Fleming, G. R. *Nature* **2005**, *434*, 625−628.

(2) Engel, G. S.; Calhoun, T. R.; Read, E. L.; Ahn, T. K.; Mančal, T.; Cheng, Y.-C.; Blankenship, R. E.; Fleming, G. R. *Nature* **2007**, *446*, 782−786.

(3) Collini, E.; Wong, C. Y.; Wilk, K. E.; Curmi, P. M. G.; Brumer, P.; Scholes, G. D. *Nature* **2010**, *463*, 644−647.

(4) Brańczyk, A. M.; Turner, D. B.; Scholes, G. D. *Ann. Phys.* **2014**, *526*, 31−49.

(5) Zigmantas, D.; Read, E. L.; Mančal, T.; Brixner, T.; Gardiner, A. T.; Cogdell, R. J.; Fleming, G. R. *Proc. Natl. Acad. Sci. U. S. A.* **2006**, *103*, 12672−12677.

(6) Rancova, O.; Abramavicius, D. *J. Phys. Chem. B* **2014**, *118*, 7533−7540.

(7) Tempelaar, R.; Jansen, T. L. C.; Knoester, J. *J. Phys. Chem. B* **2014**, *118*, 12865−12872.

(8) van der Vegte, C. P.; Prajapati, J. D.; Kleinekathöfer, U.; Knoester, J.; Jansen, T. L. C. *J. Phys. Chem. B* **2015**, *119*, 1302−1313.

(9) Olbrich, C.; Jansen, T. L. C.; Liebers, J.; Aghtar, M.; Strümpfer, J.; Schulten, K.; Knoester, J.; Kleinekathöfer, U. *J. Phys. Chem. B* **2011**, *115*, 8609−8621.

(10) McDermott, G.; Prince, S. M.; Freer, A. A.; Hawthornthwaite-Lawless, A. M.; Papiz, M. Z.; Cogdell, R. J.; Isaacs, N. W. *Nature* **1995**, *374*, 517−521.

(11) Mirkovic, T.; Ostroumov, E. E.; Anna, J. M.; van Grondelle, R.; Govindjee; Scholes, G. D. *Chem. Rev.* **2017**, *117*, 249−293.

(12) Scholes, G. D.; Gould, I. R.; Cogdell, R. J.; Fleming, G. R. *J. Phys. Chem. B* **1999**, *103*, 2543−2553.

(13) Tretiak, S.; Middleton, C.; Chernyak, V.; Mukamel, S. *J. Phys. Chem. B* **2000**, *104*, 4519−4528.

(14) Jang, S.; Dempster, S. E.; Silbey, R. J. *J. Phys. Chem. B* **2001**, *105*, 6655−6665.

(15) Novoderezhkin, V. I.; van Grondelle, R. *J. Phys. Chem. B* **2013**, *117*, 11076−11090.

(16) Jang, S.; Rivera, E.; Montemayor, D. *J. Phys. Chem. Lett.* **2015**, *6*, 928−934.

(17) Anda, A.; Hansen, T.; De Vico, L. *J. Chem. Theory Comput.* **2016**, *12*, 1305−1313.

(18) Stross, C.; van der Kamp, M. W.; Oliver, T. A. A.; Harvey, J. N.; Linden, N.; Manby, F. R. *J. Phys. Chem. B* **2016**, *120*, 11449−11463.

(19) Cupellini, L.; Jurinovich, S.; Campetella, M.; Caprasecca, S.; Guido, C. A.; Kelly, S. M.; Gardiner, A. T.; Cogdell, R.; Mennucci, B. *J. Phys. Chem. B* **2016**, *120*, 11348−11359.

(20) Damjanović, A.; Kosztin, I.; Kleinekathöfer, U.; Schulten, K. *Phys. Rev. E: Stat. Phys., Plasmas, Fluids, Relat. Interdiscip. Top.* **2002**, *65*, 031919.

(21) Cogdell, R. J.; Gall, A.; Köhler, J. *Q. Rev. Biophys.* **2006**, *39*, 227−324.

(22) Zhang, W. M.; Meier, T.; Chernyak, V.; Mukamel, S. *J. Chem. Phys.* **1998**, *108*, 7763−7774.

(23) Min Zhang, W.; Meier, T.; Chernyak, V.; Mukamel, S. *Philos. Trans. R. Soc., A* **1998**, *356*, 405−419.

(24) Yang, M.; Fleming, G. R. *Chem. Phys.* **2002**, *275*, 355−372.

(25) Novoderezhkin, V. I.; van Grondelle, R. *Phys. Chem. Chem. Phys.* **2010**, *12*, 7352−14.

(26) Ostroumov, E. E.; Mulvaney, R. M.; Cogdell, R. J.; Scholes, G. D. *Science* **2013**, *340*, 52−56.

(27) Ferretti, M.; Hendrikx, R.; Romero, E.; Southall, J.; Cogdell, R. J.; Novoderezhkin, V. I.; Scholes, G. D.; van Grondelle, R. *Sci. Rep.* **2016**, *6*, 20834.

(28) Cerullo, G.; Polli, D.; Lanzani, G.; De Silvestri, S.; Hashimoto, H.; Cogdell, R. J. *Science* **2002**, *298*, 2395−2398.

(29) Papiz, M. Z.; Prince, S. M.; Howard, T.; Cogdell, R. J.; Isaacs, N. W. *J. Mol. Biol.* **2003**, *326*, 1523−1538.

(30) Yanai, T.; Tew, D. P.; Handy, N. C. *Chem. Phys. Lett.* **2004**, *393*, 51−57.

(31) Roos, B. O. *Ab Initio Methods in Quantum Chemistry: Part II*; Wiley: Chicester, UK, 1987.

(32) Malmqvist, P.; Pierloot, K.; Shahi, A. R. M.; Cramer, C. J.; Gagliardi, L. *J. Chem. Phys.* **2008**, *128*, 204109.

(33) Curutchet, C.; Muñoz Losa, A.; Monti, S.; Kongsted, J.; Scholes, G. D.; Mennucci, B. *J. Chem. Theory Comput.* **2009**, *5*, 1838−1848.

(34) Higashi, M.; Kosugi, T.; Hayashi, S.; Saito, S. *J. Phys. Chem. B* **2014**, *118*, 10906−10918.

(35) Higashi, M.; Saito, S. *J. Chem. Theory Comput.* **2016**, *12*, 4128.

(36) Curutchet, C.; Scholes, G. D.; Mennucci, B.; Cammi, R. *J. Phys. Chem. B* **2007**, *111*, 13253−13265.

(37) Krueger, B. P.; Scholes, G. D.; Fleming, G. R. *J. Phys. Chem. B* **1998**, *102*, 5378−5386.

(38) Pajusalu, M.; Rätsep, M.; Trinkunas, G.; Freiberg, A. *ChemPhysChem* **2011**, *12*, 634−644.

(39) Mukamel, S. *Principles of Nonlinear Optical Spectroscopy*; Oxford University Press: New York, 1995.

(40) Lee, M. K.; Huo, P.; Coker, D. F. *Annu. Rev. Phys. Chem.* **2016**, *67*, 639−668.

(41) Abramavicius, D.; Palmieri, B.; Voronine, D. V.; Šanda, F.; Mukamel, S. *Chem. Rev.* **2009**, *109*, 2350−2408.

DOI: 10.1021/jacs.7b02130
J. Am. Chem. Soc. 2017, 139, 7558−7567

(42) Mukamel, S.; Abramavicius, D. *Chem. Rev.* **2004**, *104*, 2073−2098.
(43) Abramavicius, D.; Valkunas, L.; Mukamel, S. *EPL-Europhys. Lett.* **2007**, *80*, 17005.
(44) Frisch, M. J.; Trucks, G. W.; Schlegel, H. B.; Scuseria, G. E.; Robb, M. A.; Cheeseman, J. R.; Scalmani, G.; Barone, V.; Mennucci, B.; Petersson, G. A.; Nakatsuji, H.; Caricato, M.; Li, X.; Hratchian, H. P.; Izmaylov, A. F.; Bloino, J.; Zheng, G.; Sonnenberg, J. L.; Hada, M.; Ehara, M.; Toyota, K.; Fukuda, R.; Hasegawa, J.; Ishida, M.; Nakajima, T.; Honda, Y.; Kitao, O.; Nakai, H.; Vreven, T.; Montgomery, J. A., Jr.; Peralta, J. E.; Ogliaro, F.; Bearpark, M.; Heyd, J. J.; Brothers, E.; Kudin, K. N.; Staroverov, V. N.; Kobayashi, R.; Normand, J.; Raghavachari, K.; Rendell, A.; Burant, J. C.; Iyengar, S. S.; Tomasi, J.; Cossi, M.; Rega, N.; Millam, J. M.; Klene, M.; Knox, J. E.; Cross, J. B.; Bakken, V.; Adamo, C.; Jaramillo, J.; Gomperts, R.; Stratmann, R. E.; Yazyev, O.; Austin, A. J.; Cammi, R.; Pomelli, C.; Ochterski, J. W.; Martin, R. L.; Morokuma, K.; Zakrzewski, V. G.; Voth, G. A.; Salvador, P.; Dannenberg, J. J.; Dapprich, S.; Daniels, A. D.; Farkas, O.; Foresman, J. B.; Ortiz, J. V.; Cioslowski, J.; Fox, D. J. *Gaussian 09*, Revision D.01; Gaussian, Inc: Wallingford, CT, 2009.
(45) Aquilante, F.; Autschbach, J.; Carlson, R. K.; Chibotaru, L. F.; Delcey, M. G.; De Vico, L.; Fdez. Galván, I.; Ferré, N.; Frutos, L. M.; Gagliardi, L.; Garavelli, M.; Giussani, A.; Hoyer, C. E.; Li Manni, G.; Lischka, H.; Ma, D.; Malmqvist, P.; Müller, T.; Nenov, A.; Olivucci, M.; Pedersen, T. B.; Peng, D.; Plasser, F.; Pritchard, B.; Reiher, M.; Rivalta, I.; Schapiro, I.; Segarra-Martí, J.; Stenrup, M.; Truhlar, D. G.; Ungur, L.; Valentini, A.; Vancoillie, S.; Veryazov, V.; Vysotskiy, V. P.; Weingart, O.; Zapata, F.; Lindh, R. *J. Comput. Chem.* **2016**, *37*, 506−541.
(46) Guareschi, R.; Valsson, O.; Curutchet, C.; Mennucci, B.; Filippi, C. *J. Phys. Chem. Lett.* **2016**, *7*, 4547−4553.
(47) Georgakopoulou, S.; Frese, R. N.; Johnson, E.; Koolhaas, C.; Cogdell, R. J.; van Grondelle, R.; van der Zwan, G. *Biophys. J.* **2002**, *82*, 2184−2197.
(48) Read, E. L.; Schlau-Cohen, G. S.; Engel, G. S.; Georgiou, T.; Papiz, M. Z.; Fleming, G. R. *J. Phys. Chem. B* **2009**, *113*, 6495−6504.
(49) Harel, E.; Engel, G. S. *Proc. Natl. Acad. Sci. U. S. A.* **2012**, *109*, 706−711.
(50) Ma, Y.; Cogdell, R.; Gillbro, T. *J. Phys. Chem. B* **1997**, *101*, 1087−1095.
(51) Salverda, J. M.; van Mourik, F.; van der Zwan, G.; van Grondelle, R. *J. Phys. Chem. B* **2000**, *104*, 11395−11408.
(52) Ihalainen, J. A.; Linnanto, J.; Myllyperkiö, P.; van Stokkum, I. H. M.; Ücker, B.; Scheer, H.; Korppi-Tommola, J. E. I. *J. Phys. Chem. B* **2001**, *105*, 9849−9856.
(53) Pullerits, T.; Hess, S.; Herek, J. L.; Sundstrom, V. *J. Phys. Chem. B* **1997**, *101*, 10560−10567.
(54) Agarwal, R.; Yang, M.; Xu, Q.-H.; Fleming, G. R. *J. Phys. Chem. B* **2001**, *105*, 1887−1894.
(55) Wendling, M.; Mourik, F. V.; van Stokkum, I. H.; Salverda, J. M.; Michel, H.; Grondelle, R. V. *Biophys. J.* **2003**, *84*, 440−449.
(56) Hess, S.; Feldchtein, F.; Babin, A.; Nurgaleev, I.; Pullerits, T.; Sergeev, A.; Sundström, V. *Chem. Phys. Lett.* **1993**, *216*, 247−257.
(57) Ostroumov, E. E.; Mulvaney, R. M.; Anna, J. M.; Cogdell, R. J.; Scholes, G. D. *J. Phys. Chem. B* **2013**, *117*, 11349−11362.
(58) Kleinschmidt, M.; Marian, C. M.; Waletzke, M.; Grimme, S. *J. Chem. Phys.* **2009**, *130*, 044708−11.
(59) Polívka, T.; Sundström, V. *Chem. Rev.* **2004**, *104*, 2021−71.
(60) Polli, D.; Cerullo, G.; Lanzani, G.; De Silvestri, S.; Hashimoto, H.; Cogdell, R. J. *Biophys. J.* **2006**, *90*, 2486−2497.
(61) Cong, H.; Niedzwiedzki, D. M.; Gibson, G. N.; LaFountain, A. M.; Kelsh, R. M.; Gardiner, A. T.; Cogdell, R. J.; Frank, H. A. *J. Phys. Chem. B* **2008**, *112*, 10689−10703.
(62) Krueger, B. P.; Scholes, G. D.; Jimenez, R.; Fleming, G. R. *J. Phys. Chem. B* **1998**, *102*, 2284−2292.
(63) Curutchet, C.; Mennucci, B. *Chem. Rev.* **2017**, *117*, 294−343.

DOI: 10.1021/jacs.7b02130
J. Am. Chem. Soc. 2017, 139, 7558−7567